Applied Energy 255 (2019) 113822

Contents lists available at ScienceDirect

Applied Energy

journal homepage: www.elsevier.com/locate/apenergy

Broadband energy harvesting by nonlinear magnetic rolling pendulum with subharmonic resonance

Yang Kuang, Rosalie Hide, Meiling Zhu*

College of Engineering, Mathematics and Physical Sciences, University of Exeter, Exeter EX4 4QF, UK

HIGHLIGHTS

- Magnetic rolling pendulum with low mechanical loss and strong nonlinear behaviours.
- Normalised mechanical loss < 30% of those reported in the literature.
- Consecutive primary and subharmonic resonance when excitation $\geq 5\,m/s^2$.
- 1-mW-bandwidth up to 9.7 Hz with linear resonance frequency of 4.6 Hz.
- Subharmonic resonance contributes up to 2/3 of the bandwidth.

ARTICLE INFO

Keywords:
Broadband energy harvesting
Nonlinear energy harvesting
Secondary resonance
Electromagnetic
Subharmonics

ABSTRACT

Nonlinear systems may exhibit secondary resonances, which can provide an additional and thus broadened bandwidth for energy harvesting. However, the secondary resonances of nonlinear energy harvesters reported in the literature suffer from low-power output and limited bandwidth. This work proposes a novel magnetic rolling pendulum (MRP) with a large bandwidth and high power output in both primary and secondary resonances for energy harvesting. The MRP employs the rolling motion of a magnetically levitated permanent magnet with minimal mechanical damping. A prototype was fabricated and characterised. An analytical model combined with finite element analysis was developed and validated by experiment. Both experiment and simulation show that the MRP has a linear resonance frequency of 4.6 Hz and peak power of 3.7 mW. It exhibits strong nonlinear behaviours and broadband characteristics with excitation amplitude as low as $2\,m/s^2$ in the primary resonance. As the excitation amplitude is larger than $5\,m/s^2$, the secondary resonance (1/2 order subharmonics) is excited. The responses of the MRP at the subharmonic resonance take the same form as the primary resonance in terms of displacement and power outputs. This helps the subharmonic resonance to produce the same power level as the primary resonance but with a larger bandwidth. When excited at $14\,m/s^2$, the MRP shows 1-mW-bandwidth of 9.7 Hz, 2/3 of which is attributed to the subharmonic resonance.

1. Introduction

Over the past two decades, harvesting wasted or unused ambient energy has been regarded as an underpinning technology for energy-autonomous electronic devices and has thus attracted a worldwide research effort. Among various energy sources such as vibrations, temperature gradients and electromagnetic radiation, vibration energy has gained the most attention because of its high energy density and ubiquitous presence [1]. The transduction methods for vibration energy include piezoelectric, electrostatic, electromagnetic and triboelectric, all of which have been successfully implemented [2].

The majority of ambient vibrations exhibit a broadband spectrum [3], which is the main challenge for energy harvesting as most energy harvesters (EHs) are linear and display a narrow operation bandwidth. Operating a linear EH at off-resonance results in a significant reduction in power output. To address this challenge, various techniques have been proposed to broaden the operation bandwidth. Tuning the resonance frequency of linear EHs using active/passive designs [4] has been investigated but it is not efficient under random or rapidly varying frequency. Moreover, the active tuning requires a complex active circuit, which consumes an additional power. Utilising an array of EHs with different resonance frequencies [5,6] can increases the operation frequency range however it reduces the power density and scalability of the harvesters. Frequency up-conversion [7] has the ability to convert

* Corresponding author.
E-mail address: m.zhu@exeter.ac.uk (M. Zhu).

https://doi.org/10.1016/j.apenergy.2019.113822
Received 25 March 2019; Received in revised form 29 August 2019; Accepted 31 August 2019
Available online 10 September 2019

low-frequency ambient motions to high-frequency resonant vibrations of energy harvesters. This was usually implemented by impact-driven piezoelectric cantilevers [8,9], though a novel mechanism was developed by Wang et al. [10,11], who used the rectilinear motion of permanent magnets to produce a magnetic torque on a rotary energy generator to achieve the frequency up-conversion. An alternative strategy for broadband energy harvesting is to introduce nonlinearity to EHs, which, when carefully designed, has the ability to extend the operation bandwidth and has been intensively studied in recently years [12].

The type of nonlinearities used for energy harvesting is broadly classified as monostable and multi-stable, depending on the number of stable equilibrium positions. The most common approach to implement such nonlinearity in energy harvesting is to introduce a nonlinear restoring force through, for example, mechanical structures or permanent magnets. Buckled beams were used to bring bi-stability for piezoelectric [13] and electromagnetic [14] energy harvesting, although multi-stability is more common to be implemented by using nonlinear magnetic force e.g. in the form of cantilever beams with a tip magnet [15–17] or a permanent magnet levitated in a multi-well potential [18]. Monostable nonlinear systems have been realised by nonlinear magnetic forces between permanent magnets [19] and nonlinear elasticity of doubly clamped beams [20,21]. Moreover, mechanical stoppers [22,23] were found to make the stiffness of an EH piecewise and demonstrate either monostable or bistable features.

While the aforementioned nonlinear systems employ the primary resonance for energy harvesting, it is well-known that a nonlinear system may exhibit secondary resonances – the system can produce large responses at its resonance frequency f_0 when excited near the fraction integers of f_0 (f_0/n, superharmonics) or integers of f_0 (nf_0, subharmonics). Therefore, they have the potential to offer an additional bandwidth for energy harvesting and have been recently studied. Barton et al. [24] showed that superharmonics of order three ($f_0/3$) and five ($f_0/5$) could be excited on a monostable Duffing-type harvester. However, the response of the superharmonic resonance was far less than the primary resonance and appeared very similar to the linear resonance. Later, Masana and Daqaq [25] found that a bistable harvester could produce superharmonics of order two ($f_0/2$) with a lower excitation amplitude than the mono-stable counterpart. The onset of superharmonics of bistable energy harvester was further studied by Harne and Wang [26]. Leadenham and Erturk [27] observed superharmonics of order two and three on an M-shaped piezoelectric energy harvester. The main limitations of these studies are that the power level and the bandwidth of the superharmonic resonance are much lower than the primary resonance. Therefore, the benefits of the secondary resonance for energy harvesting are limited.

Furthermore, subharmonic resonance has also been exploited for energy harvesting. Arrieta et al. [28] observed 1/2 order subharmonic resonance on a bistable composite plate with piezoelectric patches attached. However, the bandwidth was not fully evaluated. Huguet et al. [29,30] developed a bistable energy harvester based on buckled beams. A 1/3 order subharmonic resonance was successfully actuated when a specially designed frequency-sweep method was used. The bistable energy harvester produced more than 100 μW over a 70 Hz frequency range, demonstrating the potential of subharmonic for broadband energy harvesting, although the power level is still in the microwatts range.

This study proposes a novel mono-stable nonlinear energy harvester design with strong nonlinear behaviours to achieve high power output and bandwidth in both the primary and subharmonic resonance regions. The nonlinear energy harvester, named as magnetic rolling pendulum (MRP) in this work, employs the rolling motion of a magnetically levitated permanent magnet with a mechanical loss that is < 30% of the magnetic levitation energy harvesters reported in the literature. The low mechanical loss increases the displacement response and thus the nonlinearity of the MRP. The MRP shows consecutive primary and subharmonic resonance region. With a linear resonance frequency of 4.6 Hz, the MRP is able to produce more than 1 mW over a 9.7 Hz frequency range, which is an increase of 194% compared to the 1-mW-bandwidth of the primary resonance. This paper details the mechanism, modelling and experimental characterisation of the MRP.

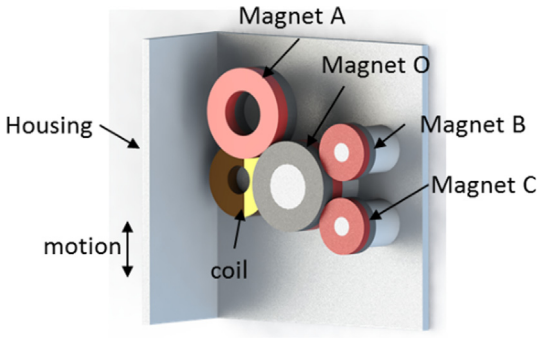

Fig. 1. A schematic of the magnetic rolling pendulum: red and grey represent the South and North poles of the magnets, respectively. The coil and magnets O, B, C are fixed to the housing while magnet A is free to move.

2. Design and fabrication

2.1. Design and considerations

The device proposed in this study is shown in Fig. 1. It consists of four permanent magnets and two coils. Permanent magnets O, B and C are fixed to the housing while the magnet A is free to move. The polarisation directions of the magnets are arranged so that A is repulsed by B and C but attracted by O. The repulsive magnetic force applied by magnets B and C to magnet A provides a nonlinear spring force, while the attractive force from magnet O constrains the motion of magnet A on the surface of magnet O. When an excitation motion is applied to the housing, magnet A experiences an inertial force. This inertial force, together with the nonlinear spring force drives magnet A to roll back and forth on the surface of magnet O. As magnet A passes by the coil, it introduces variations in the magnetic flux linkage and thus voltage in the coils through Faraday's law.

The device can be regarded as a specially designed magnetic pendulum with a rolling motion, and thus is named as magnetic rolling pendulum (MRP) in this work. The MRP has shown a broad bandwidth when subjected to parametric excitation [31]. This study focuses on the performance under direct excitation. The attractive force between the magnets A and O eliminates the use of beam/string and pivot bearing as in a traditional pendulum to keep the structure simple. In addition to providing a nonlinear spring force, magnets B and C are used to adjust the resonance frequency and the equilibrium position. The motion direction of the moving magnet in the MRP is parallel to the major surfaces of the cylindrical magnet, instead of normal to the major surfaces as in most of the magnetic levitation energy harvesting [32,33]. This helps to minimise the aerodynamic damping. A frictional force is present between magnets A and O, but this friction is a rolling friction and thus is expected to keep minimal. The nonlinear phenomenon of an oscillator based on magnetic springs is more prevalent at lower damping levels [33,34]. This is because the magnetic force is approximately linear in small displacement and the nonlinearity becomes strong when the displacement is large. Reducing the damping will help to increase the displacement and the engagement of the nonlinearity for the MRP.

2.2. Prototype fabrication

A prototype to implement the design concept is shown in Fig. 2. Parameters of the prototype, such as the size of the magnets, the shape,

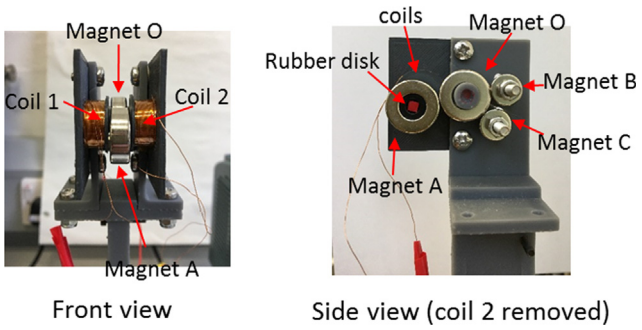

Fig. 2. A prototype of the MRP.

Table 1
Properties of the magnets and coils.

	Description	symbol	value	unit
Magnets A and O	inner radius	R_1	4.75	mm
	outer radius	R_2	9.55	mm
	thickness	t_A	6.4	mm
	mass	m	13.8	gram
Magnets B and C	inner radius	r_1	2	mm
	outer radius	r_2	6	mm
	thickness	t_B	4	mm
Coils 1 and 2	inner radius	R_{c1}	3	mm
	outer radius	R_{c2}	7.9	mm
	thickness	t_c	7	mm
	Coil position	d_{gap}	1.7	mm
	Coil resistance	R_i	10	Ω

size and position of the coils can be optimised to maximise the power generation. As this study aims to investigate the mechanism, the optimisation was not performed at present stage. The four magnets are ring-shaped N42 Neodymium magnets (Magnet Expert LTD, UK) with dimensions listed in Table 1. The size of magnets B and C are kept small and placed close to each other to allow a large travelling space for magnet A. Moreover, the position of magnets B and C were chosen so that the equilibrium position of magnet A is vertically aligned to magnet O. Two coils are placed symmetrically along the path of magnet A. The gap between the coil and magnet A is $d_g = 1.7$ mm. Each coil is made of 500 turns of a 200 μm copper wire. A rubber disk with a red tape was glued to the hollow of magnet A to facilitate tracking the position of magnet A by video analysis, which will be further explained later.

3. Modelling of the MRP

3.1. Analytical model of the system dynamics

The schematic of the analytic model is presented in Fig. 3. Magnet A rolls on the surface of the central magnet O with an angular velocity of $\dot{\varphi}$ with respect to its centre A. The angular displacement of point A with respect to the centre of the magnet O is denoted as θ. The position angles of the magnets B and C are $\alpha = 0.13$ rad and $\beta = 0.76$ rad, respectively. This leads to an equilibrium position of magnet A at $\theta = 0$. The total magnetic force experienced by the magnet A is projected to the tangent and normal directions as F_{mt} and F_{mn}, respectively. F_f is the frictional force. $F_i = mA_0\cos(2\pi ft)$ is the inertial force due to input acceleration with amplitude of A_0 and excitation frequency f.

The following set of equations can be obtained by applying Newton's second law of motion:

$$\sum F_t = mA_0 \ \cos(2\pi ft) \ cos\theta + F_{mt} - mgcos\theta - F_f - c_1\dot{\theta} = m\cdot a_t = m\cdot 2R_2\ddot{\theta} \quad (1)$$

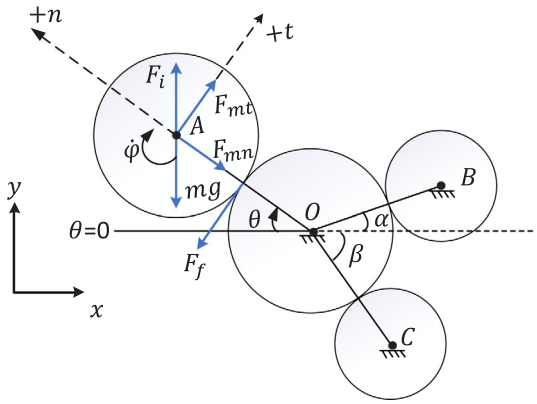

Fig. 3. Schematics of the analytical model of the system.

$$\sum M_A = F_f R_2 - c_2\dot{\varphi}R_2 = I_A\ddot{\varphi} \quad (2)$$

where $\sum F_t$ is the resultant force along the tangent axis (+ t); R_2 is the outer radius of magnets O and C; a_t is the tangent acceleration of magnet A with respect to O and equals to $2R_2\ddot{\theta}$; $\sum M_A$ is the resultant torque about A; I_A is the moment of inertia of magnet A with respect to its centre A. c_1 and c_2 are the damping factors. Assuming that magnet A rolls without slipping, the relationship between $\dot{\varphi}$ and $\dot{\theta}$ is

$$2R_2\cdot\dot{\theta} = R_2\cdot\dot{\varphi} \quad (3)$$

Substituting Eq. (2) and (3) into Eq. (1), the dynamics of the system can be expressed as

$$(2mR_2 + \frac{2I_A}{R_2})\ddot{\theta} + c_d\dot{\theta} - F_{mt} + mgcos\theta = mA_0 \ \cos(\omega t) \ cos\theta \quad (4)$$

The damping factor of the system c_d is the sum of the mechanical damping c_m and electromagnetic dampingc_e. Eq. (4) is apparently nonlinear. The nonlinearity is introduced by the nonlinear magnetic force F_{mt}, which will be discussed in details later and the modulation of $cos\theta$ to the inertial force and gravity.

θ in Eq. (4) is limited by magnets B and C. For the present prototype with position angle $\alpha = 0.13$ rad and $\beta = 0.76$ rad, θ is between -1.47 to 2.02 rad. When θ reaches the limits, collision between magnets occurs. Although the collision will be quite gentle as the magnets act as 'soft stoppers' [35], losses in kinetic energy are expected. This can be accounted for by

$$\dot{\theta}(t^+) = -(1-\gamma)\dot{\theta}(t^-) \quad (5)$$

$\dot{\theta}(t^-)$ and $\dot{\theta}(t^+)$ are the velocity of magnet A before and after the collision. γ is a loss factor between 0 and 1.

The open-circuit voltage produced in one coil by the magnet A is

$$V_{OC} = -N\frac{d\Phi_B}{dt} = -N\cdot\frac{d\Phi_B}{d\theta}\cdot\frac{d\theta}{dt} = -N\dot{\theta}\cdot\frac{d\Phi_B}{d\theta} \quad (6)$$

where N is the number of turns in the coil; $\Phi_B$is the magnetic flux through each turn of the coil and is a function of θ. When the coil is connected to a load resistor matching its internal resistanceR_i, the average power dissipated in the load resistor in a time period of T is

$$P = \frac{1}{T}\int_0^T \frac{V_{OC}^2}{4R_i}dt \quad (7)$$

The magnetic force F_{mt}, the magnetic flux Φ_B and the damping factor c_d must be determined prior to numerically solving the above equations to simulate the performance of the MRP. In this study, F_m and Φ_B were derived by finite element analysis while c_d was measured from experiment.

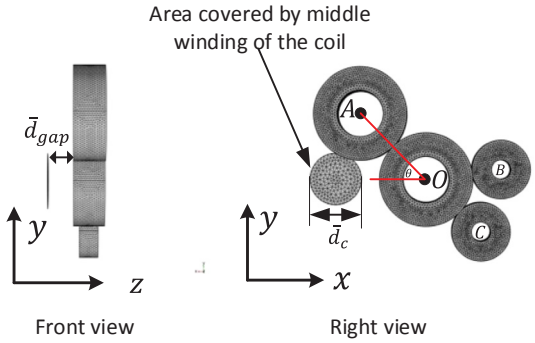

Fig. 4. FE model to simulate the magnetic force and flux.

3.2. Finite element analysis

An FE model of the MRP was developed in COMSOL Multiphysics to compute the magnetic force F_{mt} and the induced magnetic flux Φ_B in the coil. The physical model (Fig. 4) consists of the four ring-shaped permanent magnets placed in the centre of an air enclosure ($120 \times 120 \times 120\,mm^3$, not shown in Fig. 4). The dimensions of the magnets are aligned with those in Table 1. A remanent flux density of 1.28 T (specified by the supplier) along the z-axis was assigned to magnets A, B and C, while -1.28 T was assigned to magnet O. A circular surface parallel to xy plane and with a diameter of $\bar{d}_c = (R_{c2} + R_{c1})$ was created at a distance of $\bar{d}_{gap} = (d_{gap} + t_c/2)$ from the magnet A. This surface is the area covered by the middle winding of the coil and the magnetic flux through it will be used to represent the average flux through each winding of the coil. The position of the magnet A was varied by changingθ. For eachθ, the magnetic force and the magnetic flux were simulated by the stationary analysis of COMSOL.

4. Experimental testing of the MRP

Experimental testing was performed on the prototype presented in Fig. 2. The MRP was installed on a base made of plastic and with a height of 15 cm, as shown in Fig. 5. The base was then mounted on an electromagnet shaker (V20, Data Physics). The reason to introduce a long base is to exclude any magnetic interaction between the shaker and the MRP.

In free vibration testing, magnet A was displaced manually from its equilibrium position and then released to ring down. During this process, the coils were open-circuited to eliminate any electric damping. The motion of magnet A was recorded by the camera of a smart phone (iPhone 6 plus) at 240 frames per second. The recorded video was then processed by a video analysis software, Tracker 5.0 (Open Source Physics), to extract the angular displacement of magnet A with respect

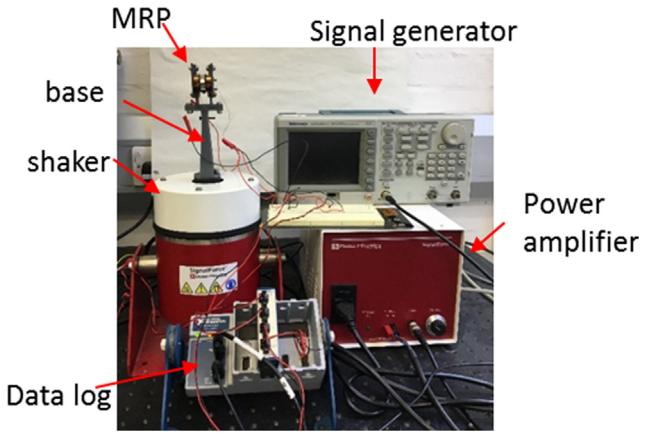

Fig. 5. Experimental setup to measure the power generation of the MRP.

to the centre of magnet O, i.e. the value of θ. To fully expose magnet A to the camera, one coil of the MRP was removed during the vibration test, as shown in the side view of Fig. 2. Moreover, a rubber disk was glued in the hollow of magnet A and a small red tape was stick to the centre. The position of the red tape therefore reflects the position of magnet A and can be tracked during video analysis.

In power generation testing, a signal generator, which was controlled by a LabVIEW program running on a PC, applied the sinusoidal excitation signal to the shaker through a power amplifier. Each of the two coils was separately connected to a 10 Ω load resistor, which is the internal resistance of the coils. The voltage across the load resistors were measured by a data log through the LabVIEW program to calculate the average power generation. Prior to measuring the power generation, the excitation voltages required by the shaker to produce acceleration of 1 to 14 m/s^2 at frequencies between 4 and 20 Hz was measured with the aid of an accelerometer (5 g ceramic shear accelerometer, Kistler). Following that, the power output of the MRP was measured by the method of bidirectional frequency sweeps at constant acceleration. During both up- and down-frequency sweeps, the frequency of the excitation voltage was varied in steps of 0.1 Hz and each frequency was held for 30 s to allow the motion of magnet A to reach steady state. At the same time as the frequency was varied, the voltage amplitude was adjusted according to the prior measurements to maintain a constant input acceleration.

5. Results and discussions

5.1. Results of finite element modelling

The magnetic force F_{mt} simulated by the FE analysis is presented in Fig. 6(a), which can be approximated by Eq. (8). The parameters of Eq. (8) were determined by least-square curve-fitting in MATLAB. The relationship between F_{mt} and θ is approximately linear when $|\theta|$ is small and moderate (about $|\theta| < 1$) and becomes increasingly nonlinear as $|\theta|$ is further increased. Therefore, to produce strong nonlinear behaviours, the displacement has to be large enough, which can be achieved by increasing the actuation amplitude or reducing the damping level. The magnetic force is slightly asymmetrical about $\theta = 0$ because the position angles α and β (see Fig. 3) are not equal. This asymmetry is also reflected in the fitting equation of the magnetic force, where quadratic and fourth-order terms are present. The presence of the quadratic nonlinear term is the perquisite of 1/2 order subharmonics [36].

$$F_{mt} = \sum_{i=0}^{5} a_i \theta^i \tag{8}$$

The magnetic flux Φ_B through the middle winding of the coil is shown in Fig. 6(b). The relationship between Φ_B and θ can be mathematically fitted by Eq. (9). The values of the parameters in Eqs. (8) and (9) are listed in Table 2.

$$\Phi_B = \sum_{i=0}^{7} A_i \cos(i\omega_1 \theta) \tag{9}$$

5.2. Free vibration of the MRP

The video footage recording the free motion of magnet A and processed by Tracker 5.0 is attached as free motion clip.gif. A typical frame of the footage is shown in Fig. 7. The origin of the coordinate system is at the centre of magnet O. The red quadrilaterals represent the trajectory of magnet A, recognised by Tracker 5.0. The coordinates of these quadrilaterals were exported to calculate the angular position of magnet A, which is compared with the simulation results in Fig. 8.

The free motion simulation was performed by numerically solving Eq. (4) with $A_0 = 0$. The damping factor c_m was set to 3.3×10^{-4} Ns/rad, corresponding to a mechanical damping ratio of 0.018. The

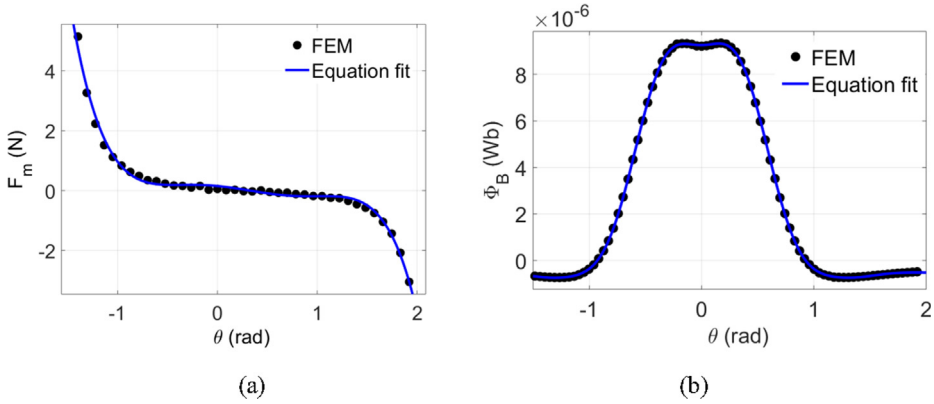

Fig. 6. (a) Magnetic force and (b) magnetic flux of the MRP simulated by finite element analysis.

Table 2
The values of the parameters for magnetic force and flux determined by curve-fitting in MATLAB.

parameters	values	parameters	values	parameters	values
a_0	0.145	a_5	-0.492	A_5	-3.95×10^{-7}
a_1	-0.245	A_1	2.12×10^{-6}	A_6	-2.75×10^{-7}
a_2	-0.555	A_2	4.20×10^{-6}	A_7	-8.4×10^{-8}
a_3	0.151	A_3	1.96×10^{-6}	ω_1	1.636
a_4	0.820	A_4	1.02×10^{-7}		

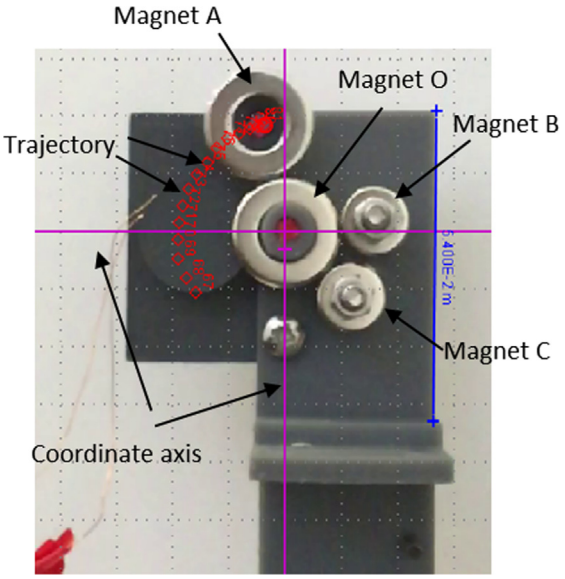

Fig. 7. A typical frame of the processed video footage recording the motion of magnet A.

simulated free motion shows good agreement with experiment in both time- and frequency-domains, which validates the value of the damping factor and the magnetic force simulated by the finite element model. The multiple peaks in the frequency spectrum is because the stiffness and thus the resonance frequency of the system varies with θ.

The simulated frequency spectrums of the free vibration with different initial displacements are presented in Fig. 9. As the initial displacement is 0.2 rad, the frequency spectrum of the free vibration demonstrates that of a linear system with a resonance frequency of 4.6 Hz, suggesting that at small vibration amplitude, the MRP can be approximated as a linear system.

5.3. Simulated and measured energy harvesting performance

5.3.1. Characteristics of primary and subharmonic resonances

The simulated and measured electric power outputs of the MRP when excited at 9 m/s^2 and connected to the 10 Ω load resistor are compared in Fig. 10. In simulation, Eqs. (4) and (5) were numerically solved to compute θ and $\dot{\theta}$, which were then substituted to Eqs. (6) and (7) and (9) to compute the voltage and power generation. The damping factor c_d was adjusted to be 3.9×10^{-4} Ns/rad to account for the electric damping. The loss factor γ was set to 0.1. The value of γ does not affect the trend of the response, which will be discussed in Section 5.3.2. In experiment, the result below 7 Hz was not measured for the present excitation amplitude because of the limitation of the shaker used. Considering the good coincidence between simulation and experiment, the response of the MRP in the untested frequency range is expected follow the trend of the simulation.

As shown in Fig. 10, the MRP exhibits hysteretic responses when excitation frequency $f > 5.9$ Hz, where two stable responses co-exist. In the hysteretic region, the power of the up-sweep is always higher than the down-sweep, suggesting hardening nonlinearity of the MRP. Since high power output is desirable, the rest of this paper focuses on analysing the behaviours of the MRP in the high-power branch, i.e. the performance measured or simulated in frequency up-sweep condition.

In Fig. 10, as the excitation frequency f increases, the power output experiences a sharp jump-up around the linear resonance frequency $f_0 = 4.6$ Hz. Then it increases steadily until it reaches the first peak, immediately following which the first steep jump-down occurs at f_1. The frequency region from low frequency until f_1 is the primary resonance region, where the frequency of the displacement equals to the excitation frequency. This can be verified by the measured and simulated displacement of the MRP presented in Fig. 11(a) and (b). When the MRP is excited at 7 Hz, both simulated and measured displacements are exactly at 7 Hz as expected. The good agreement between simulation and experiment implies that both the magnetic force and magnetic flux simulated by the finite element model are valid. The main frequency component of the voltage is at 14 Hz, as shown in Fig. 11(c), because each cycle of displacement introduces two cycles of magnetic flux variations, which is a common feature of electromagnetic energy harvesters.

After the first jump-down, the power produced by the MRP increases again with f until the second peak and jump-down are observed at around f_2. The frequency range between f_s and f_2, i.e. from the onset of the power increase following the first jump-down to the second jump-down, is the secondary resonance region. In this region, the displacement frequency is mainly half of the excitation frequency, suggesting that the secondary resonance is a 1/2 order subharmonic resonance originated from the quadratic nonlinearity. A typical example is shown in Fig. 12. When the MRP is excited at 14 Hz, the displacement in both experiment and simulation is mainly at 7 Hz.

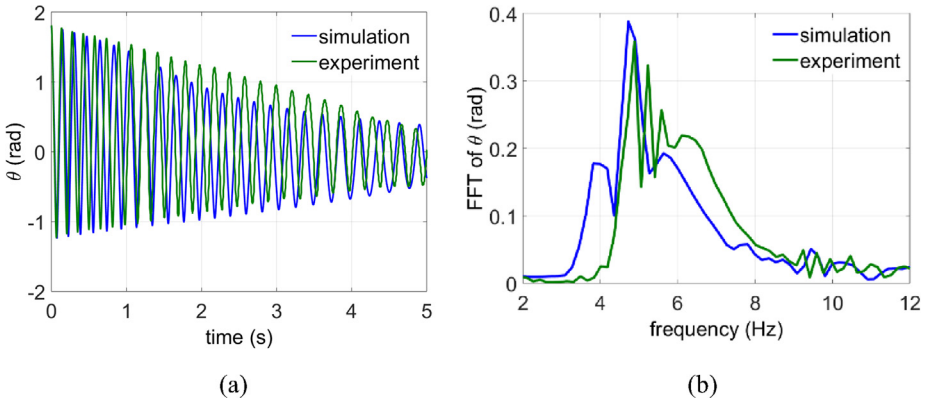

Fig. 8. Comparison of the simulated and measured free vibration of the MRP (a) time domain variation of θ (b) frequency spectrum of θ.

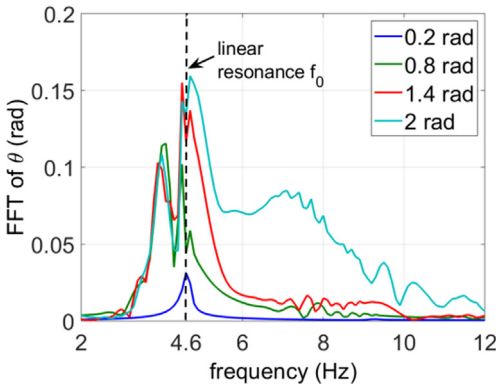

Fig. 9. Simulated frequency spectrums of the free vibration with initial displacements from 0.2 to 2 rad.

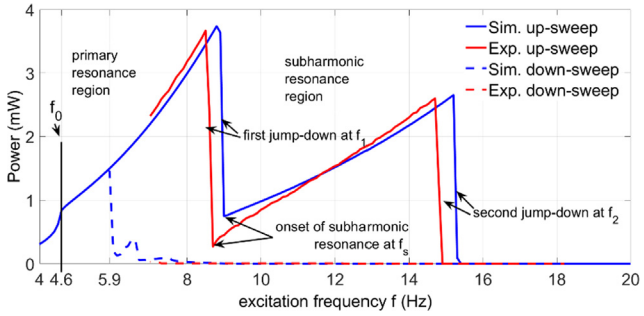

Fig. 10. Simulated and measured electric power output of the MRP subjected to harmonic excitation at 9 m/s^2 in frequency up- and down-sweep.

The subharmonic resonances of nonlinear energy harvesters reported in the literature usually produce much smaller responses than the primary resonance. In contrast, the subharmonic resonance of the MRP actuated at $2f$ always produces almost identical outputs as the primary resonance actuated at f across the whole subharmonic resonance region, which can be easily verified by the results presented in Figs. 10–12. The subharmonic resonance always takes the same form as the primary counterpart and looks like a recurrence of the primary resonance at doubled excitation frequencies. This unique phenomenon is advantageous for energy harvesting because the subharmonic resonance can produce the same power level as the primary resonance but with a larger bandwidth.

5.3.2. *Effects of excitation amplitude*

The simulated electric power outputs of the MRP excited at different acceleration levels are presented in Fig. 13(a). Generally, with larger A_0, the resonance region extends to a broader range, leading to a larger bandwidth. The nonlinear behaviour of the MRP—the bending of the frequency-response curve is observed with acceleration amplitude A_0 being as low as 2 m/s^2. As A_0 is increased to ≥5 m/s^2, the subharmonic resonance appears and starts at 9 Hz. This suggests that the subharmonic can only be excited when the excitation is sufficiently large.

As A_0 increases from 2 m/s^2, the first jump-down frequency f_1 first increases and then saturates at around 8.9 Hz. The increases of f_1 is because the corresponding jump-downs are caused by bending of frequency-response curve as a result of the hardening nonlinearity. This kind of jump-down frequency increases with excitation amplitude and decreases with the damping level, which has been well documented in the literature [36]. The saturation is because the corresponding jump-downs are a result of the collision between magnet A and B when magnet A reaches its upper position limit. This can be demonstrated by the maximum displacements of the MRP shown in Fig. 13(b). As A_0 ≥

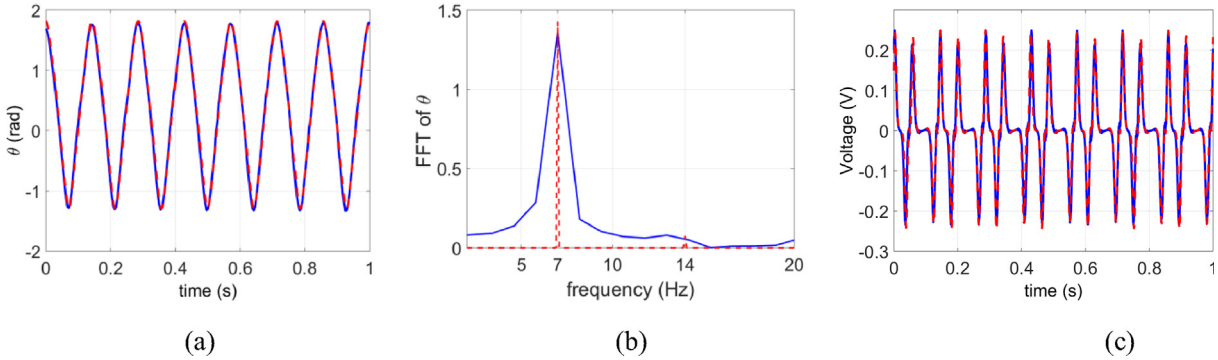

Fig. 11. (a) Displacement, (b) FFT of the displacement and (c) voltage across the load resistor when the MRP is excited at 7 Hz, 9 m/s^2. Solid and blue: experiment; dash and red: simulation.

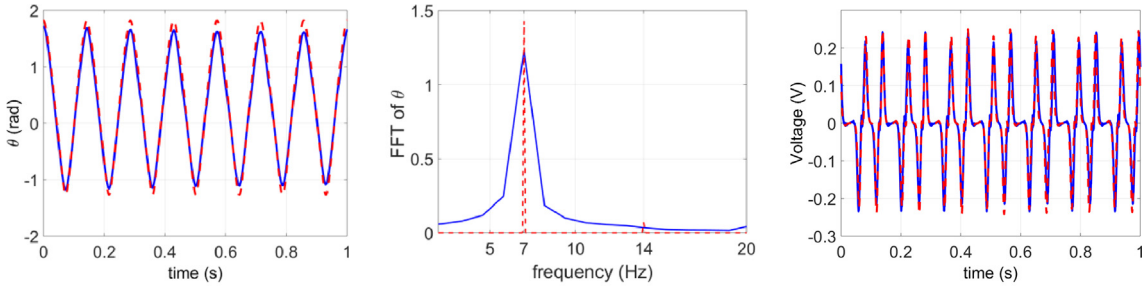

Fig. 12. (a) Displacement, (b) FFT of the displacement and (c) voltage across the load resistor when the MRP is excited at 14 Hz, 9 m/s^2. Solid and blue: experiment; dash and red: simulation.

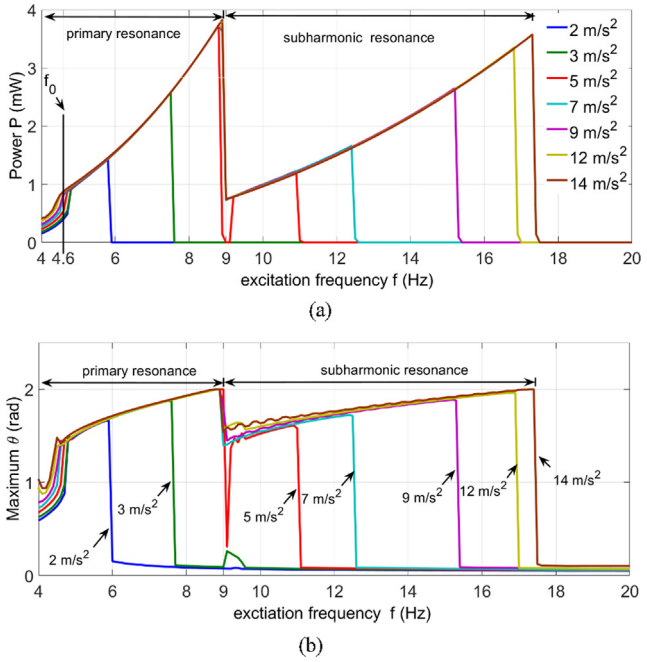

Fig. 13. Simulated (a) electric power outputs and (b) maximum displacement of the MRP excited at different acceleration amplitudes in frequency up-sweeps.

5 m/s^2, the peak displacement reaches the position limit of 2.02 rad at 8.9 Hz. As a result of the disturbance and energy loss from the collision, the MRP jumps to a lower energy state and enters the subharmonic resonance. The loss factor was found to affect the number of collisions before the jump. However, as long as there is a loss, the jump will eventually occur. The second jump-down frequency f_2 follows the similar trend of f_1. The collision occurs at 17.5 Hz withA_0 = 14 m/s^2. Following that collision, the vibration of the MRP jumps to near zero and no lower order of subharmonic resonance is observed at higher frequency range.

When the resonance is excited, the displacement of the magnet is mostly larger than 1.5 rad even when the A_0 is as low as 2 m/s^2. This large displacement is resulted from the low mechanical damping of the MRP and helps to enhance the nonlinear behaviour as the nonlinearity increases progressively with displacement (Fig. 7). The engagement of the strong nonlinearity leads increased power bandwidth. Another phenomenon caused by the strong nonlinearity is that the displacement and power level is independent of the acceleration amplitude, except in the region around the linear resonance frequency. Similar behaviours have also been reported by other monostable nonlinear energy harvesters [20,37].

The measured electric power outputs at different excitation amplitudes are presented in Fig. 14. The experiment results match the

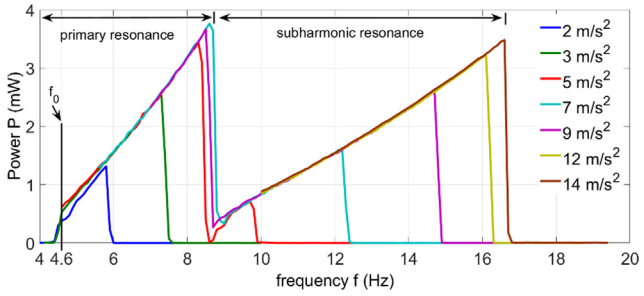

Fig. 14. Measured electric power outputs of the MRP excited at different acceleration amplitudes in frequency up-sweeps.

simulation quite well at each excitation level. The experiment shows peak power output of 3.7 mW at 8.6 Hz, compared with 3.8 mW at 8.9 Hz in simulation. The subharmonic resonance in experiment starts at 8.7 Hz, compared to 9 Hz in simulation. The slight difference in the simulated and measured onset frequency of the subharmonic resonance is caused by minor difference in the upper limit of the displacement between experiment and simulation.

5.3.3. Further discussion

As a result of the bended frequency–response curve and the appearance of the subharmonic resonance, the bandwidth of the MRP is increased. In light of the double-resonance characteristics of the MRP, a 1-mW-bandwidth is used to evaluate the bandwidth, which is the frequency range with power output over 1 mW. The measured bandwidth of the MRP is presented in Table 3. As A_0 is increased from 2 to 5 m/s^2, the 1-mW-bandwidth is increased from 0.4 to 3.1 Hz and the contribution is solely from the primary resonance. As A_0 further increases, the subharmonic resonance starts to contribute to the bandwidth. The contribution of the subharmonic resonance to the bandwidth exceeds that of the primary resonance when $A_0 \geq$ 8 m/s^2. When excited at 14 m/

Table 3
Measured peak power and 1-mW-bandwidth of the MRP at different acceleration amplitudes.A_0

A_0 (m/s^2)	Peak Power (mW)	1-mW-bandwidth (Hz)		
		Primary resonance	Subharmonic resonance	Total
2	1.3	0.4	–	0.4
3	2.6	2.1	–	2.1
5	3.5	3.1	0	3.1
7	3.8	3.4	1.8	5.2
8	3.7	3.3	3.2	6.5
9	3.7	3.3	4.5	7.8
12	3.7	3.3	5.9	9.2
14	3.7	3.3	6.4	9.7

Table 4
Comparison of the bandwidth of the MRP with the state-of-the-art broadband energy harvesters.

Reference	f_0 (Hz)	Acceleration A_0(m/s^2)	P_{max}(mW)	Half-power-bandwidth (Hz)	Bandwidth ratioΛ	Figure of Merit (μW·s^4/m^2)
MRP	4.6	2	1.3	0.9	0.2	64
MRP	4.6	3	2.6	1.7	0.37	106
MRP	4.6	5	3.5	2.1	0.46	63
MRP	4.6	9	3.7	4.2	0.91	41
MRP	4.6	14	3.7	6.0	1.26	24
Stanton [40]	15	10	0.7	2.5	0.17	1.2
Soliman [22]	95	1.4	0.11	9.4	0.10	5.6
Cottone [14]	48	2.8	2	9.9	0.21	52.6
Basset [41]	162	10	0.002	40	0.25	0.005
Podder [16]	35.2	5	0.025	7.68	0.22	0.2

Table 5
Comparison of mechanical damping in nonlinear broadband energy harvesters.

Reference	f_0	ζ_m	ζ_{normal}
MRP	4.6	0.018	1.0
Constantinou 2012 [35]	37	0.029	13.7
Nammari 2017 [33]	32	0.130	52.1
	32	0.060	24.3
Lee et al. 2010 [42]	8.5	0.031	3.3
Cottone et al. 2014 [14]	48	0.017	10.4

s^2, the 1-mW-bandwidth is as large as 9.7 Hz and the contribution of the subharmonic resonance is nearly twice of the primary resonance.

The bandwidth of the MRP is compared with the state-of-the-art broadband energy harvesters in Table 4, where the traditional half-power-bandwidth is used. The bandwidth ratio Λ is the ratio of half-power-bandwidth to the linear resonance frequencyf_0. The figure of merit [14] for broadband energy harvesting is defined as

$$Figure\ \ of\ \ Merit = \Lambda \times \frac{P_{max}}{A_0^2} \tag{10}$$

where P_{max} is the maximum power output. The MRP in this work shows the largest bandwidth ratio and figure of merit. This is a result of the strong nonlinear behaviours promoted by low mechanical damping. The mechanical damping ratio ζ_m of the MRP was compared with some of magnetic levitation energy harvesters in Table 5. Because the damping ratio is dependent on the frequency, a normalised damping ratio is used for the comparison, which is defined as [38]

$$\zeta_{normal} = 4\pi\zeta_m f_0 \tag{11}$$

The normalised damping ratio of the MRP is 1.0, which is less than 30% of the values of other energy harvesters.

The resonance range and the bandwidth make the MRP suitable for energy harvesting from low-frequency vibrations. One application scenario is harnessing the vibration of rail tacks caused by passing trains, which has main frequency components in the range of 1–30 Hz [39]. The harvested energy can be used to power wireless railway condition monitoring sensors.

6. Conclusions

In this work, a novel magnetic rolling pendulum (MRP) for broadband energy harvesting has been developed, modelled and characterised. Both analytical simulation and experiment characterisation were performed to assess the performance. The MRP demonstrated a subharmonic resonance with large power output and bandwidth, in addition to the high-performance primary resonance, and therefore has a great potential for broadband energy harvesting.

The magnetic spring force of the MRP simulated by finite element analysis showed the presence of a quadratic nonlinear term, which is the origin of the 1/2 subharmonics observed on the MRP. In both simulation and experiment, the MPR possessed nonlinear behaviours and thus broadband characteristics in the primary resonance with excitation acceleration A_0 being as low as 2 m/s^2. As A_0increases, the mW-bandwidth of primary resonance increases up to 3.4 Hz. When $A_0 \geq$ 5 m/s^2, the subharmonic resonance appeared, which was identified as the 1/2 order subharmonic resonance since the response is mainly at half of the excitation frequency. The subharmonic resonance responses of the MRP actuated at a frequency $2f$ were always nearly the same as the primary resonance response actuated at f. As a result, the subharmonic resonance produced high power output and actively contributed to the bandwidth. As $A_0 \geq$ 8 m/s^2, the contribution of the subharmonic resonance to the mW-bandwidth exceeds that of the primary one, thus greatly increased the total bandwidth. At $A_0 =$ 14 m/s^2, the MRP showed an mW-bandwidth of 9.7 Hz, 67% of which is attributed to the subharmonic resonance. The resonance range and broad bandwidth make the MRP suitable for energy harvesting from low-frequency and broadband vibration sources such as rail track vibration caused by passing trains.

Acknowledgements

The authors would like to acknowledge the finical support from Engineering and Physical Sciences Research Council of UK (EP/K020331/1 and EP/K017950/2).

Appendix A. Supplementary material

Supplementary data to this article can be found online at https://doi.org/10.1016/j.apenergy.2019.113822.

References

[1] Kuang Y, Ruan T, Chew ZJ, Zhu M. Energy harvesting during human walking to power a wireless sensor node. Sens Actuators A 2017;254:69–77.
[2] Abdelkareem MA, et al. Vibration energy harvesting in automotive suspension system: a detailed review. Appl Energy 2018;229:672–99.
[3] Beeby SP, et al. A comparison of power output from linear and nonlinear kinetic energy harvesters using real vibration data. Smart Mater Struct 2013;22(7):075022.
[4] Zhu D, Roberts S, Tudor MJ, Beeby SP. Design and experimental characterization of a tunable vibration-based electromagnetic micro-generator. Sens Actuators A 2010;158(2):284–93.
[5] Foisal ARM, Hong C, Chung G-S. Multi-frequency electromagnetic energy harvester using a magnetic spring cantilever. Sens Actuators A 2012;182:106–13.
[6] Song H-C, et al. Broadband dual phase energy harvester: Vibration and magnetic field. Appl Energy 2018;225:1132–42.
[7] Yang K, Meiling Z. Characterisation of a knee-joint energy harvester powering a wireless communication sensing node. Smart Mater Struct 2016;25(5):055013.
[8] Yang K, Zhihao Y, Meiling Z. Design and characterisation of a piezoelectric knee-joint energy harvester with frequency up-conversion through magnetic plucking. Smart Mater Struct 2016;25(8):085029.
[9] Zhang J, Qin L. A tunable frequency up-conversion wideband piezoelectric vibration energy harvester for low-frequency variable environment using a novel impact-and rope-driven hybrid mechanism. Appl Energy 2019;240:26–34.
[10] Deng W, Wang Y. Non-contact magnetically coupled rectilinear-rotary oscillations to exploit low-frequency broadband energy harvesting with frequency up-conversion. Appl Phys Lett 2016;109(13):133903.
[11] Chen J, Wang Y. A dual electromagnetic array with intrinsic frequency up-conversion for broadband vibrational energy harvesting. Appl Phys Lett 2019;114(5):053902.

[12] Daqaq MF, Masana R, Erturk A, Quinn DD. On the role of nonlinearities in vibratory energy harvesting: a critical review and discussion (in English). Appl Mech Rev 2014;66(4). Art. no. 040801.
[13] Zhu Y, Zu J. A magnet-induced buckled-beam piezoelectric generator for wideband vibration-based energy harvesting. J Intell Mater Syst Struct 2014. p. 1045389X14541498.
[14] Cottone F, Basset P, Vocca H, Gammaitoni L, Bourouina T. Bistable electromagnetic generator based on buckled beams for vibration energy harvesting. J Intell Mater Syst Struct 2014;25(12):1484–95.
[15] Zhou S, Cao J, Inman DJ, Lin J, Liu S, Wang Z. Broadband tristable energy harvester: modeling and experiment verification. Appl Energy 2014;133:33–9.
[16] Podder P, Amann A, Roy S. Combined effect of bistability and mechanical impact on the performance of a nonlinear electromagnetic vibration energy harvester. IEEE/ASME Trans Mechatron 2016;21(2):727–39.
[17] Vocca H, Neri I, Travasso F, Gammaitoni L. Kinetic energy harvesting with bistable oscillators. Appl Energy 2012;97:771–6.
[18] Gao M, Wang Y, Wang Y, Wang P. Experimental investigation of non-linear multistable electromagnetic-induction energy harvesting mechanism by magnetic levitation oscillation. Appl Energy 2018;220:856–75.
[19] Aldawood G, Nguyen HT, Bardaweel H. High power density spring-assisted nonlinear electromagnetic vibration energy harvester for low base-accelerations. Appl Energy 2019;253:113546.
[20] Mallick D, Amann A, Roy S. A nonlinear stretching based electromagnetic energy harvester on FR4 for wideband operation. Smart Mater Struct 2014;24(1):015013.
[21] Liu W, Yuan Z, Zhang S, Zhu Q. Enhanced broadband generator of dual buckled beams with simultaneous translational and torsional coupling. Appl Energy 2019;251:113412.
[22] Soliman MS, Abdel-Rahman EM, El-Saadany EF, Mansour RR. A design procedure for wideband micropower generators. J Microelectromech Syst 2009;18(6):1288–99.
[23] Wang X, et al. A frequency and bandwidth tunable piezoelectric vibration energy harvester using multiple nonlinear techniques. Appl Energy 2017;190:368–75.
[24] Barton DA, Burrow SG, Clare LR. Energy harvesting from vibrations with a nonlinear oscillator. J Vib Acoust 2010;132(2):021009.
[25] Masana R, Daqaq MF. Energy harvesting in the super-harmonic frequency region of a twin-well oscillator. J Appl Phys 2012;111(4):044501.
[26] Harne R, Wang K. On the fundamental and superharmonic effects in bistable energy harvesting. J Intell Mater Syst Struct 2014;25(8):937–50.
[27] Leadenham S, Erturk A. Nonlinear M-shaped broadband piezoelectric energy harvester for very low base accelerations: primary and secondary resonances. Smart Mater Struct 2015;24(5):055021.
[28] Arrieta A, Hagedorn P, Erturk A, Inman D. A piezoelectric bistable plate for nonlinear broadband energy harvesting. Appl Phys Lett 2010;97(10):104102.
[29] Huguet T, Badel A, Lallart M. Exploiting bistable oscillator subharmonics for magnified broadband vibration energy harvesting. Appl Phys Lett 2017;111(17):173905.
[30] Huguet T, Badel A, Druet O, Lallart M. Drastic bandwidth enhancement of bistable energy harvesters: Study of subharmonic behaviors and their stability robustness. Appl Energy 2018;226:607–17.
[31] Kuang Y, Zhu M. Parametrically excited nonlinear magnetic rolling pendulum for broadband energy harvesting. Appl Phys Lett 2019;114(20):203903.
[32] Apo DJ, Priya S. High power density levitation-induced vibration energy harvester. Energy Harvest Syst 2014;1(1–2):79–88.
[33] Nammari A, Bardaweel H. Design enhancement and non-dimensional analysis of magnetically-levitated nonlinear vibration energy harvesters. J Intell Mater Syst Struct 2017;28(19):2810–22.
[34] Mann B, Sims N. Energy harvesting from the nonlinear oscillations of magnetic levitation. J Sound Vib 2009;319(1–2):515–30.
[35] Constantinou P, Mellor PH, Wilcox PD. A magnetically sprung generator for energy harvesting applications. IEEE/ASME Trans Mechatron 2012;17(3):415–24.
[36] Nayfeh AH, Mook DT. Nonlinear oscillations. John Wiley & Sons; 2008.
[37] Liu H, Tay CJ, Quan C, Kobayashi T, Lee C. Piezoelectric MEMS energy harvester for low-frequency vibrations with wideband operation range and steadily increased output power. J Microelectromech Syst 2011;20(5):1131–42.
[38] Palagummi S, Yuan F. An optimal design of a mono-stable vertical diamagnetic levitation based electromagnetic vibration energy harvester. J Sound Vib 2015;342:330–45.
[39] Cleante V, Brennan M, Gatti G, Thompson D. On the target frequency for harvesting energy from track vibrations due to passing trains. Mech Syst Sig Process 2019;114:212–23.
[40] Stanton SC, McGehee CC, Mann BP. Nonlinear dynamics for broadband energy harvesting: investigation of a bistable piezoelectric inertial generator (in English). Phys D-Nonlinear Phenomena Article 2010;239(10):640–53.
[41] Basset P, et al. Electrostatic vibration energy harvester with combined effect of electrical nonlinearities and mechanical impact. J Micromech Microeng 2014;24(3):035001.
[42] Lee C, Stamp D, Kapania NR, Mur-Miranda JO. Harvesting vibration energy using nonlinear oscillations of an electromagnetic inductor. Energy harvesting and storage: materials, devices, and applications, vol. 7683. International Society for Optics and Photonics; 2010. p. 76830Y.